Lattice-Boltzmann method for simulating spherical bubbles with no tangential stress boundary conditions

Xiaolong Yin, Donald L. Koch,* and Rolf Verberg
School of Chemical and Biomolecular Engineering, Cornell University, Ithaca, New York 14853
(Received 29 June 2005; published 1 February 2006)

A lattice-Boltzmann boundary rule has been developed to recover the slip boundary condition at a liquid-gas interface. This rule enables one to use a single-component lattice-Boltzmann model to simulate bubbly flows where bubbles are nearly spherical and coalescence is prohibited. Numerical tests showed this method to be robust and accurate in simulating both steady and unsteady flows around spherical bubbles in the Reynolds number range $0<\mathrm{Re}<30$.

DOI: 10.1103/PhysRevE.73.026301 PACS number(s): 47.55.D−, 47.15.−x, 47.11.−j

I. INTRODUCTION

Bubbly flows are frequently encountered in chemical engineering applications where contact between gases and liquids is desired to promote heat and mass transport. Typically bubble suspensions differ from suspensions of solid particles in three important ways. First, the fluid velocity can "slip" at the gas-liquid interface; second, the gas-liquid interface can deform, and therefore a bubble does not necessarily maintain a predetermined shape; third, bubbles can coalesce and break, leading to a bubble size distribution that is continuously evolving in time. The presence of a slip boundary condition at the gas-liquid interface greatly reduces the vorticity transported from the bubble interface into the liquid at high Reynolds numbers. Consequently the drag on a bubble is much lower than that on a solid particle and the average flow properties of a bubble suspension may differ substantially from those of solid particle suspensions. To understand the consequences of this distinction in a simple setting, it is desirable to study a bubble suspension in which the bubbles remain spherical and do not coalesce.

In this paper, we present a numerical method to simulate a special class of bubbly flows in which the bubbles are nearly spherical and where bubble coalescence is suppressed. Such flows are of fundamental interest since they allow us to isolate the effect of the slip boundary condition. And they are also accessible to laboratory experiments, as discussed in detail below.

The deformability of bubbles in a flow dominated by fluid inertia can be characterized by the Weber number $\mathrm{We}=\rho U a^2/\sigma$, where ρ is the density of the liquid, a is the bubble radius, U is the bubble velocity relative to the mean velocity of the suspension or mixture, and σ is the surface tension of the liquid-gas interface. For an inertia-dominated flow with $\mathrm{We}\ll 1$, the fluid pressure does not deform the bubbles. A suspension of air bubbles with diameters of about 1 mm in clean water are a good example of an inertia-dominated low-Weber-number system. For slower flows, it is important that the capillary number (ratio of viscous stresses to surface tension) and the Bond number (ratio of gravity to surface tension) be small to assure small deformation of the bubbles. Alternatively, one can consider the Morton and Eotvos numbers of the bubble suspension, which form the basis of the empirical diagram of regimes of bubble deformation presented in Clift, Grace, and Weber [1].

Coalescence can be prevented by adding either electrolytes [2] or surfactants to the liquid. It is known that surfactants create a surface tension gradient, which immobilizes the gas-liquid interface and increases the drag [1]. Electrolytes, unlike surfactants, do not cause this so-called Marangoni effect; thus, the slip boundary condition at the gas-liquid interface is maintained. The use of electrolytes to stabilize bubbly suspensions was demonstrated recently by Zenit *et al.* [3], who used a magnesium sulfate solution (0.05 mol/l) to suppress coalescence and were able to maintain a high degree of monodispersity up to 15% volume fractions. Hence, the class of bubbly suspension we study is also experimentally relevant.

Due to the bubble's small deformability and resistance to coalescence, it is most convenient to model this type of bubble suspension as a system of hard spheres with slip boundaries. This model enables us to use a single-component fluid mechanics solver to simulate the flow in the continuous phase and eliminates the need for a second fluid component, which is commonly used in simulations of drops and bubbles. As a result, the computational cost is reduced and the robustness of the computation is improved.

For bubbly suspensions with spherical, noncoalescing bubbles, it is possible to derive the averaged equations of motion from first principles, provided that the Reynolds number is either very small or very large. Here the Reynolds number is defined as $\mathrm{Re}=2\rho U a/\eta$. For $\mathrm{Re}\ll 1$, the flow is dominated by viscous effects and governed by the Stokes equation. These equations are linear and can be solved directly by using a multipole expansion method (see, for example, Mo and Sangani [4]). For $\mathrm{Re}\gg 1$, as pointed out by Moore [5,6] and later validated experimentally by Duineveld [7], the vorticity is confined to a small boundary layer near the liquid-gas interface. The fluid velocity outside this boundary layer can be written as the gradient of a potential (hence the name "potential flow"), which is governed by Laplace's equation. Since Laplace's equation is linear, one can solve the potential flow interactions among spherical

*Corresponding author. Electronic address: dlk15@cornell.edu.

bubbles and derive the equations of motion for such suspensions [8–14]. In the experiments of Zenit *et al.* [3], nitrogen bubbles with diameters of about 1 mm in size were generated and left to rise in a vertical channel filled with water. Here, $\mathrm{Re}=O(100)$ and $\mathrm{We}=O(1)$, making these experiments the ideal tool to validate the predictions of the potential flow theory. Indeed, good qualitative agreement was found between the results and the theoretical predictions of Spelt and Sangani [14].

In the intermediate-Reynolds-number regime, however, we cannot use the potential flow approximation; nor can we ignore the presence of inertial effects. This makes it difficult to solve the many-body interaction problem and close the equations of motion. One has to resort to either well-controlled experiments or direct numerical simulations. Past numerical work on bubbly flows in the intermediate-Reynolds-number regime include the works of Esmaeeli and Tryggvason [15,16], Bunner and Tryggvason [17,18], Sankaranarayanan *et al.* [19,20], Sankaranarayanan and Sundaresan [21], Tölke *et al.* [22], and Inamuro *et al.* [23]. These authors used different approaches, but all of them were based on two-component models—one component represents the continuous phase; another component, with its density and viscosity much smaller than those of the continuous phase, represents the droplets or bubbles. Typically, the density and viscosity ratios are of order 0.01 to 0.02, with the exception of Inamuro *et al.* [23], who was able to implement a projection method into a two-component lattice-Boltzmann model and reduced the density ratio to $\rho_b/\rho=0.001$. For the sake of comparison, the density and viscosity ratios for air in water under normal conditions are $O(10^{-3})$ and $O(10^{-2})$, respectively.

Using a finite-difference method with a front tracking technique, Esmaeeli and Tryggvason studied the rise of an array of deformable, nearly spherical bubbles for $\mathrm{Re}=O(1)$ [15] and for deformable, ellipsoidal bubbles at $\mathrm{Re}\approx 20$ [16]. Bunner and Tryggvason [17,18] later used the same method to study the rise of a relatively large number of nearly spherical bubbles with moderate Reynolds numbers $\mathrm{Re}\approx 20$. In their method, the bubbles have well-defined boundaries. Thus coalescence can be prevented by simply not allowing the boundaries to merge when they closely approach each other. It is then possible to study the suspension's properties over relatively long times.

Sankaranarayanan *et al.* [19,20], Sankaranarayanan and Sundaresan [21], Tölke *et al.* [22], and Inamuro *et al.* [23] all used a two-component lattice-Boltzmann model for an immiscible binary mixture to simulate the rise of an array of bubbles. This model leads to the formation of bubbles that are by nature deformable, although the bubble's interface is diffusive and often suffers from spurious velocities [24]. As it is difficult to implement a plausible mechanism to prevent the bubbles from coalescing, in [19–21] only the flow around a single bubble in a periodic box was studied in detail. From the simulations, the drag coefficient, the virtual mass coefficient, and the lift force were obtained and these parameters were then used to propose a set of averaged equations of motion for bubble suspensions at moderate Reynolds numbers.

Our approach differs from the aforementioned studies in that we only attempt to solve the flow in the continuous phase. When the flow drives bubbles into contact, the normal relative velocity of the bubbles is reversed instantaneously as it would be for elastic hard spheres, thereby preventing coalescence without the need to account for the detailed deformation involved during the collision process. The slip boundary condition is imposed on the bubble surface by ensuring explicitly in the lattice-Boltzmann models that there is neither a tangential stress at the surface nor a normal velocity relative to the surface. In this model the bubbles have sharp, well-defined interfaces, as opposed to the diffuse interfaces in the conventional two-phase lattice-Boltzmann models. Our model performs well for density ratios ρ_b/ρ as low as 1.2×10^{-3}, which is the approximate value for air in water under normal conditions. We obtained accurate results from a range of test cases, suggesting that our model captures the essential physics of a bubbly flow and that it can be used as an accurate method to simulate bubbly flows in the intermediate-Reynolds-number regime.

This paper is organized as follows. In Sec. II, we give a brief overview of the lattice-Boltzmann method. In Sec. III, we derive our boundary rule to recover the slip boundary condition at the liquid-gas interface. In Sec. IV, we discuss three test cases: (i) unidirectional flow in a system bounded by a free surface from above and driven by an impulsively started solid plate from below, (ii) creeping flow past a cubic array of bubbles, and (iii) intermediate-Reynolds-number steady and unsteady flows around an isolated bubble. The first two test cases have analytical solutions; the last one has been studied extensively in the past [1,25–29]. In Sec. V, we conclude with a summary and a discussion of our main results.

II. LATTICE-BOLTZMANN METHOD

Our numerical method is based on a lattice-Boltzmann model for particle-laden flows as reviewed in detail by Ladd and Verberg [30]. The lattice-Boltzmann method is different from most conventional numerical methods in fluid dynamics in the sense that it does not involve a direct solution of the continuum equations. Rather, it uses a simplified kinetic model to simulate the motion of fluid "particles" on a simple lattice such that the averaged properties of the system obey the desired Navier-Stokes equation. It is also different from molecular simulations since it does not deal with individual molecules but rather with their velocity distribution function. The lattice-Boltzmann method is therefore a mesoscopic model, whose local rules are guided by molecular phenomena, but whose emergent behavior captures the continuum properties of the system. Due to this mesoscopic nature, the lattice-Boltzmann method is very versatile, leading to a wide variety of models for a range of different applications [30–33].

The fundamental quantity in the lattice-Boltzmann method, as in all kinetic models, is the single-particle velocity distribution function $n_i(\mathbf{r},t)\equiv n(\mathbf{r},\mathbf{c}_i,t)$, describing the density of fluid particles at position $\mathbf{r}$ and time t, with a velocity $\mathbf{c}_i$. Here, $\mathbf{r}$, $\mathbf{c}_i$, and t are discrete variables, but the distribution function itself is continuous. In three dimensions, $\mathbf{r}$ takes on the values from a space-filling cubic lattice.

We used a discrete set of 19 velocities to represent the velocity space. These velocities correspond to fluid particles that can either stay at their current lattice position ($\mathbf{c}=[000]$) or propagate to the nearest ($\mathbf{c}=[100]$) and next-nearest ($\mathbf{c}=[110]$) neighbors on the cubic lattice. The macroscopic properties—the density ρ, the momentum density $\mathbf{j}$, and the momentum flux $\mathbf{\Pi}$—are then moments of n_i over the discrete velocity space: i.e.,

$$\rho = \sum_i n_i,$$

$$\mathbf{j} = \sum_i n_i \mathbf{c}_i = \rho \mathbf{u},$$

$$\mathbf{\Pi} = \sum_i n_i \mathbf{c}_i \mathbf{c}_i. \tag{1}$$

Here, $\mathbf{u}$ is the local fluid velocity.

The time evolution of the velocity distribution function is governed by a discretized Boltzmann equation [34] and occurs as a sequence of two steps, a collision step and a propagation step:

$$n_i(\mathbf{r} + \mathbf{c}_i \Delta t, t + \Delta t) = n_i^*(\mathbf{r},t) = n_i(\mathbf{r},t) + \Delta_i[\mathbf{n}(\mathbf{r},t)]. \tag{2}$$

In the collision step, all populations at $\mathbf{r}$ undergo instantaneous molecular collisions, producing the post-collision distribution $n_i^*(\mathbf{r},t)$. Here, the collision operator Δ_i represents the change in n_i due to this collision process. In the propagation step, the post-collision populations travel to neighboring nodes in the direction of their velocities $\mathbf{c}_i$. The time step Δt and the lattice spacing Δx are chosen such that fluid particles always reach the next node in the directions of their velocities in precisely one time step.

Each n_i can be divided into an equilibrium part and a nonequilibrium part: $n_i \equiv n_i^{eq} + n_i^{neq}$, where the n_i evolve in time toward local equilibrium. For flow velocities much less than the speed of sound, the equilibrium part can be obtained by expanding the Maxwell-Boltzmann distribution as a Taylor series in the local velocity $\mathbf{u}$: i.e.,

$$n_i^{eq} = a^{c_i}\left[\rho + \frac{\mathbf{j}\cdot\mathbf{c}_i}{c_s^2} + \frac{\rho \mathbf{u}\mathbf{u}:(\mathbf{c}_i\mathbf{c}_i - c_s^2\mathbf{I})}{2c_s^4}\right], \tag{3}$$

where $\mathbf{I}$ is the unit tensor. Here c_s is the isothermal speed of sound in the fluid, which is chosen as $c/\sqrt{3}$, with $c=\Delta x/\Delta t$. The weights a^{c_i} describe the fraction of molecules moving in the direction of $\mathbf{c}_i$. They only depend on the magnitude of the velocity and are equal to $\frac{1}{3}$, $\frac{1}{18}$, and $\frac{1}{36}$ for the [000], [100], and [110] directions, respectively. The expansion in Eq. (3) is truncated at $O(\mathbf{u}^2)$, which turns out to be sufficient to simulate the Navier-Stokes equation [35]. The second moment of the equilibrium distribution function gives the familiar Eulerian expression for the stress tensor,

$$\mathbf{\Pi}^{eq} = \sum_i n_i^{eq} \mathbf{c}_i \mathbf{c}_i = p\mathbf{I} + \rho \mathbf{u}\mathbf{u}, \tag{4}$$

with an ideal-gas equation of state $p=\rho c_s^2$.

The collision operator can take any form subject to the constraints of mass and momentum conservation. The most widely used one is the so-called single-exponential relaxation time collision operator $\Delta_i = -n_i^{neq}/\tau$ [36–38]. However, for reasons discussed in detail by Ladd and Verberg [30] and d'Humières *et al.* [39] (among others), we used the more general collision operator [30]

$$\Delta_i = \sum_j \mathcal{L}_{ij} n_j^{neq}(\mathbf{r},t). \tag{5}$$

Here, $\mathcal{L}_{ij}$ are the matrix elements of the linearized collision operator $\mathcal{L}$ that must satisfy the following eigenvalue equations

$$\sum_i \mathcal{L}_{ij} = 0,$$

$$\sum_i \mathbf{c}_i \mathcal{L}_{ij} = 0,$$

$$\sum_i \overline{\mathbf{c}_i \mathbf{c}_i} \mathcal{L}_{ij} = \lambda \overline{\mathbf{c}_j \mathbf{c}_j},$$

$$\sum_i c_i^2 \mathcal{L}_{ij} = \lambda_B c_j^2, \tag{6}$$

where $\overline{\mathbf{c}_i \mathbf{c}_i}$, indicates the traceless part of $\mathbf{c}_i \mathbf{c}_i$. The first two equations follow from conservation of mass and momentum, and the last two equations describe the relaxation of the viscous stress tensor. The eigenvalues λ and λ_B must lie in the range $(-2,0)$ and are related to the shear and bulk viscosities through [30]

$$\eta = -\rho c_s^2 \Delta t \left(\frac{1}{\lambda} + \frac{1}{2}\right),$$

$$\eta_B = -\frac{2\rho c_s^2 \Delta t}{3}\left(\frac{1}{\lambda_B} + \frac{1}{2}\right). \tag{7}$$

Mass and momentum are conserved quantities and therefore unmodified during the collision step; hence, $\Sigma_i n_i^{neq} = \Sigma_i n_i^{neq} \mathbf{c}_i = 0$, as can be readily verified from Eqs. (1) and (3). However, the second moment of n_i^{neq}—i.e., $\mathbf{\Pi}^{neq} \equiv \mathbf{\Pi} - \mathbf{\Pi}^{eq} = \Sigma_i n_i^{neq} \mathbf{c}_i \mathbf{c}_i$—is in general nonzero and modified during the collision step. Hence, its post-collision value $\mathbf{\Pi}^{neq,*}$ depends on the particular choice of the collision operator; in our case [see Eqs. (5) and (6)], this results in [30]

$$\mathbf{\Pi}^{neq,*} = (1+\lambda)\overline{\mathbf{\Pi}^{neq}} + \frac{1}{3}(1+\lambda_B)(\mathbf{\Pi}^{neq}:\mathbf{I})\mathbf{I}, \tag{8}$$

where $\overline{\mathbf{\Pi}^{neq}}$ stands for the traceless part of $\mathbf{\Pi}^{neq}$. The post-collision distribution function in Eq. (3) can then be written as

$$n_i^* = a^{c_i}\left[\rho + \frac{\mathbf{j}\cdot\mathbf{c}_i}{c_s^2} + \frac{(\rho\mathbf{u}\mathbf{u} + \mathbf{\Pi}^{neq,*}):(\mathbf{c}_i\mathbf{c}_i - c_s^2\mathbf{I})}{2c_s^4}\right]. \tag{9}$$

Thus, Eqs. (8) and (9) determine explicitly the post-collision distribution function in terms of moments of the precollision distribution function.

Equation (9) describes the evolution of the lattice-Boltzmann model in the absence of external forces. If an

external force density is present—e.g., a pressure gradient or a gravitational field—the evolution of the lattice-Boltzmann model includes additional contributions as discussed in [30].

By using multi-time-scale analysis, one can show that the lattice-Boltzmann model as described in this section recovers the incompressible Navier-Stokes equation in the limit of small Mach number $M=u/c_s \ll 1$ [30]. In our simulation we kept M below 0.1. This limits u to a fairly small number; hence, in order to increase the range of Reynolds numbers we decreased the viscosity and increased the bubble radii. Furthermore, since compressibility effects are of order M^2, we set $\lambda_B=-1$, such that the isotropic part of $\mathbf{\Pi}^{neq}$ relaxes to zero in one lattice-Boltzmann time step.

III. BOUNDARY CONDITION

During the propagation step of the lattice-Boltzmann algorithm, the post-collision populations either stay at the same node or propagate to a neighboring node depending on their velocities. If this propagation would cause fluid particles to cross a fluid-solid or fluid-bubble interface, a boundary condition must be applied. For a solid interface, a large number of different approaches are available in the literature [32,34,40–43] (among others). A particularly simple and robust means of imposing a no-slip boundary condition at a solid-fluid interface is the so-called link-bounce-back rule [32,34]. Here, the interface is represented by boundary nodes, defined as those positions located halfway along each link that connects neighboring solid and fluid nodes. Populations of fluid particles that are propagating toward a boundary node are reflected back in the direction from which they came with a modified velocity distribution function given by [32]

$$n_{i'}(\mathbf{r},t+\Delta t) = n_i^*(\mathbf{r},t) - \frac{2\rho a^{c_i}\mathbf{c}_i\cdot\mathbf{u}_b(\mathbf{r}_b,t)}{c_s^2}. \tag{10}$$

Here $n_{i'}$ is the population with a velocity in the opposite direction of the incoming velocity ($\mathbf{c}_{i'}=-\mathbf{c}_i$), and $\mathbf{r}_b=\mathbf{r}+\frac{1}{2}\mathbf{c}_i\Delta t$ and $\mathbf{u}_b$ are the respective position and velocity of the boundary node. Equation (10) results in a no-slip boundary condition that is satisfied at the boundary node—i.e., halfway between the fluid node and its neighboring solid node with a relative error that is of first order in the spatial discretization [44].

To simulate bubbly flows, we need to develop a method that enforces a free-slip boundary condition at the fluid-bubble interface. Similar to the link-bounce-back rule for fluid-solid interfaces, we represent the bubble interface by boundary nodes that are located halfway along each link that crosses the fluid-bubble interface. We then assume again that it is possible to write

$$n_{i'}(\mathbf{r},t+\Delta t) = n_i^*(\mathbf{r},t) + \delta_i(\mathbf{r},t). \tag{11}$$

Here, δ_i has to be determined such that Eq. (11) recovers the slip boundary condition at all boundary nodes. Hence, the condition of zero normal velocity,

$$\mathbf{n}\cdot\mathbf{u} = \mathbf{n}\cdot\mathbf{u}_b, \tag{12}$$

and the condition of zero tangential stress,

$$\mathbf{n}\cdot\boldsymbol{\sigma}\cdot(\mathbf{I}-\mathbf{nn}) = \mathbf{0}, \tag{13}$$

must be satisfied onthe entire bubble surface. Here $\mathbf{n}$ is the unit normal vector to the interface pointing into the fluid, $\mathbf{u}_b$ is the bubble velocity, $\mathbf{u}$ is the local fluid velocity, and $\boldsymbol{\sigma}$ is the local fluid viscous stress tensor, all calculated at the bubble interface. Equations (12) and (13) originate from the boundary conditions of velocity and shear stress at a fluid-fluid interface [1] in the limit that the viscosity of the fluid inside the spherical interface is vanishingly small. In general both velocity and shear stress must be continuous across the interface. However, when the viscosity of the fluid inside is negligible compared to that of the fluid outside—e.g., an air bubble in a liquid—the shear stress inside the bubble is very small and can be neglected. In this case, the shear stress of the fluid outside will also vanish at the interface. As a result, no boundary condition is required on the tangential velocity of the fluid outside the bubble, since the tangential velocity of the gas can adjust to any tangent fluid velocity outside without causing a significant shear stress. The normal velocity, however, is still constrained by the kinematic condition, which require the fluid velocity normal to the interface to equal the normal velocity of the interface. Finally, in a real bubble, the difference in the normal stress across the interface is balanced by the surface tension. Our assumption that the bubble is always spherical implies that the surface tension is always sufficient to equal the normal stress difference with minimal bubble deformation. Thus we do not have a constraint on the normal stress of the fluid outside.

Our derivation of the free-slip boundary condition closely follows that of Ladd and Verberg [30] for the link-bounce-back rule for solid-fluid interfaces. Here, we need the fact that the multi-time-scale analysis shows that $\boldsymbol{\sigma}$ in Eq. (8) equals $-\mathbf{\Pi}^{neq}$ [30] and has the form

$$\boldsymbol{\sigma} = -\mathbf{\Pi}^{neq} = -\frac{\rho c_s^2\Delta t}{\lambda}\left[(\boldsymbol{\nabla}\mathbf{u}+\boldsymbol{\nabla}\mathbf{u}^{\mathrm{T}}) - \frac{2}{3}(\boldsymbol{\nabla}\cdot\mathbf{u})\mathbf{I}\right] - \frac{2\rho c_s^2\Delta t}{3\lambda_v}(\boldsymbol{\nabla}\cdot\mathbf{u})\mathbf{I}. \tag{14}$$

Substituting Eq. (14) into Eqs. (8) and (9) and using the fact that the velocity distribution function can be expanded in terms of its moments as

$$n_i = a^{c^i}\left[\rho + \frac{\mathbf{j}\cdot\mathbf{c}_i}{c_s^2} + \frac{(\mathbf{\Pi}-\rho c_s^2\mathbf{I}):(\mathbf{c}_i\mathbf{c}_i-c_s^2\mathbf{I})}{2c_s^4}\right] \tag{15}$$

yields a post-collision distribution expressed in terms of the local velocity gradients:

$$n_i^*(\mathbf{r},t) = n_i(\mathbf{r},t) + \frac{\rho a^{c_i}\Delta t}{c_s^2}(\mathbf{c}_i\cdot\boldsymbol{\nabla}\mathbf{u}\cdot\mathbf{c}_i - c_s^2\,\boldsymbol{\nabla}\cdot\mathbf{u}). \tag{16}$$

Substituting Eq. (14) into Eq. (13) implies that the no-tangential-stress boundary condition at the fluid-bubble interface can also be expressed in terms of the local velocity gradients:

$$\mathbf{n}\cdot(\nabla\mathbf{u}+\nabla\mathbf{u}^{\mathrm{T}})\cdot(\mathbf{I}-\mathbf{nn})=\mathbf{0}. \tag{17}$$

Using Eqs. (16) and (17) and then decomposing the local velocity gradient into components that are normal and tangential to the fluid-bubble interface, we obtain

$$n_i^*(\mathbf{r},t)=n_i(\mathbf{r},t)+\frac{\rho a^{c_i}\Delta t}{c_s^2}[(\mathbf{c}_i\cdot\mathbf{n})^2(\mathbf{nn}:\nabla\mathbf{u}) + \mathbf{c}_i\cdot\mathbf{P}_\parallel\cdot\nabla\mathbf{u}\cdot\mathbf{P}_\parallel\cdot\mathbf{c}_i], \tag{18}$$

with $\mathbf{P}_\parallel\equiv(\mathbf{I}-\mathbf{nn})$ being an operator that projects a vector into the plane tangent to the interface. Here, we neglected terms proportional to $\nabla\cdot\mathbf{u}$, which are of second order in the Mach number and can therefore be ignored in our simulations.

In the link-bounce-back rule, the adjustment to the reflected populations [the second term on the right-hand side of Eq. (10)] assures that any distribution at node $\mathbf{r}$ that is consistent with the boundary node velocity $\mathbf{u}_b$ is stationary with respect to interactions with the boundary nodes. This requires that $n_{i'}(\mathbf{r},t+\Delta t)=n_{i'}(\mathbf{r},t)$ for any velocity $\mathbf{u}_b$ at the fluid-solid interface. To simulate bubbles, we require the same condition in order to obtain δ_i in Eq. (11), resulting in

$$\delta_i(\mathbf{r},t)=n_{i'}(\mathbf{r},t)-n_i^*(\mathbf{r},t), \tag{19}$$

for the boundary conditions in Eqs. (12) and (13). Substituting Eq. (18) into Eq. (19) and using Eq. (15) to relate two populations n_i and $n_{i'}$ with equal and opposite velocities at the same position and time results in

$$\delta_i=-\frac{2\rho a^{c_i}}{c_s^2}\mathbf{c}_i\cdot\mathbf{u}-\frac{\rho a^{c_i}\Delta t}{c_s^2}[(\mathbf{c}_i\cdot\mathbf{n})^2(\mathbf{nn}:\nabla\mathbf{u}) + \mathbf{c}_i\cdot\mathbf{P}_\parallel\cdot\nabla\mathbf{u}\cdot\mathbf{P}_\parallel\cdot\mathbf{c}_i]. \tag{20}$$

Assuming that the fluid velocity varies over a length scale that is large compared to the lattice spacing, the fluid velocity at the boundary can be expanded in a Taylor series such that, to leading order in the velocity gradients,

$$\mathbf{u}(\mathbf{r}_b,t)=\mathbf{u}(\mathbf{r},t)+\frac{\Delta t}{2}\mathbf{c}_i\cdot\ \nabla\mathbf{u}|_{\mathbf{r},t}. \tag{21}$$

Applying the boundary condition for the normal velocity at the interface [Eq. (12)] leads to

$$\mathbf{n}\cdot\mathbf{u}_b(\mathbf{r}_b,t)=\mathbf{n}\cdot\mathbf{u}(\mathbf{r},t)+\frac{\Delta t}{2}\mathbf{n}\cdot\ (\mathbf{c}_i\cdot\nabla\mathbf{u})|_{\mathbf{r},t} \approx\mathbf{n}\cdot\mathbf{u}(\mathbf{r},t)+\frac{\Delta t}{2}(\mathbf{c}_i\cdot\mathbf{n})\ (\mathbf{nn}:\nabla\mathbf{u})|_{\mathbf{r},t}, \tag{22}$$

with $\mathbf{u}_b$ again the velocity of the interface at the boundary node. Here, we neglected gradients in the tangential direction of the normal component of the velocity gradient, which is correct for a flat interface and applies to leading order to curved interfaces as well (i.e., for bubbles with radii that are large compared to the lattice spacing). Decomposing $\mathbf{c}_i\cdot\mathbf{u}$ in Eq. (20) into a sum of products of the normal and tangential components and using Eq. (22) to express the normal component of the fluid velocity at the interface in terms of the normal component of the boundary node velocity yields

$$\delta_i=-\frac{2\rho a^{c_i}}{c_s^2}\left(\mathbf{c}_i\cdot\mathbf{nn}\cdot\mathbf{u}_b+\mathbf{c}_i\cdot\mathbf{P}_\parallel\cdot\mathbf{u}+\frac{\Delta t}{2}\mathbf{c}_i\cdot\mathbf{P}_\parallel\cdot\nabla\mathbf{u}\cdot\mathbf{P}_\parallel\cdot\mathbf{c}_i\right). \tag{23}$$

The first term in Eq. (23) is similar to the change in population density in the link-bounce-back rule for the no-slip boundary condition except that only the normal components of the fluid and bubble velocities are involved. This reflects the fact that the tangential velocity at a free-slip boundary is not specified by the boundary conditions. The second and third terms on the right-hand side of Eq. (23) are adjustments to the population density that are obtained by using the zero-tangential-stress boundary condition and by using a tangential velocity at the boundary that is obtained from a Taylor-series expansion of the velocity field about the fluid node.

Using $\mathbf{j}=\rho\mathbf{u}$ and Eq. (14) to express $\mathbf{u}$ and $\nabla\mathbf{u}$ back in terms of the first and second moments of the velocity distribution function, we finally arrive at

$$n_{i'}(\mathbf{r},t+\Delta t)=n_i^*(\mathbf{r},t)-\frac{2a^{c_i}}{c_s^2}[\mathbf{c}_i\cdot\mathbf{nn}\cdot\rho\mathbf{u}_b(\mathbf{r}_b,t) + \mathbf{c}_i\cdot\mathbf{P}_\parallel\cdot\mathbf{j}(\mathbf{r},t)]-\frac{\lambda a^{c_i}}{2c_s^4}\mathbf{c}_i\cdot\mathbf{P}_\parallel\cdot\overline{\mathbf{\Pi}^{neq}}(\mathbf{r},t)\cdot\mathbf{P}_\parallel\cdot\mathbf{c}_i. \tag{24}$$

Similar to the link-bounce-back rule for solid interface, this result is explicit in time and first-order accurate in the spatial discretization with relative errors that are of second order in the Mach number.

IV. NUMERICAL TESTS

We present three test problems to validate the new free-slip boundary rule in Eq. (24) as derived in the previous section. The first problem is a unidirectional flow above an impulsively started plate. Due to the two-dimensional nature and the simple geometry, it is possible to show the detailed actions of the propagation and bounce-back rules such that one can observe the differences between the no-slip bounce-back rule and the new rule for slip boundaries. In addition, since an analytical solution is available, this problem provides an opportunity to verify both the transient and steady-state behavior of the simulation. The second problem is the creeping flow around a cubic array of bubbles. In this problem, the model's ability to handle curved interfaces at a low Reynolds number is tested. This problem also serves as a calibration, from which the accuracy of the method can be improved. The last problem is a study of bubbles rising under gravity at moderate Reynolds numbers. By comparing the acceleration and terminal drag to results from the literature we validate the ability of our model to simulate steady and unsteady bubbly flows where inertial effects are important.

A. Planar flow with a free surface driven by a flat plate

In this section we consider a two-dimensional unidirectional flow of a fluid bounded by a solid plate from below (at

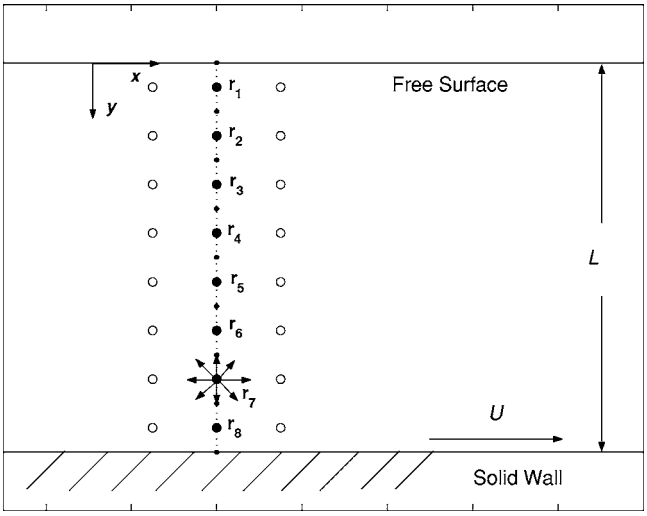

FIG. 1. The computational domain between the free surface and the solid wall is divided equally into eight segments. The solid circles are the fluid nodes $\mathbf{r}_1,\ldots,\mathbf{r}_8$, and the open circles are their periodic images.

$y=L$) and a free surface from above (at $y=0$) (see Fig. 1). Initially, the entire fluid is at rest. At time $t=0$, the solid wall is set in motion with a constant velocity U in the x direction. The fluid is accelerated by the momentum transferred from the solid wall to the fluid and quickly develops into a plug flow because the free surface does not provide resistance of any kind. In this problem, the full Navier-Stokes equations reduce to a parabolic partial differential equation with a Fourier series solution,

$$\frac{u_x(y,t)}{U} = 1 - \sum_{k=0}^{\infty} \frac{4(-1)^k}{(2k+1)\pi} e^{-(2k+1)^2\pi^2\eta t/4\rho L^2} \times \cos\left[\frac{(2k+1)\pi y}{2L}\right], \tag{25}$$

against which the accuracy of our bounce-back rule can be tested directly.

Since the flow is planar, we project the three-dimensional 19-velocity lattice-Boltzmann model onto the xy plane to a two-dimensional nine-velocity lattice-Boltzmann model. The resulting set of velocities and their associated weights are summarized in Table I. We used $\rho=36$ and $\Delta x=\Delta t=1$, giving $c_s^2=1/3$. Since the flow properties only depend on the y coordinate, we only need a single column of N lattice nodes. Periodic boundary conditions are then applied in the x direction. Furthermore, since both the link-bounce-back rule for a fluid-solid boundary and our rule for a fluid-gas boundary simulate an interface position that is halfway between the fluid node and its neighboring solid or gas node, we position the first and last nodes half a lattice unit away from the computational domain boundaries (see Fig. 1 for $L=N=8$). The fluid is at rest at $t=0$—i.e., $\mathbf{j}(\mathbf{r}_j,0)=0$ and $\mathbf{\Pi}(\mathbf{r}_j,0)=p\mathbf{I}$ throughout the entire fluid domain. Hence, the initial populations at each fluid node are simply $n_i(\mathbf{r}_j,0)=\rho a^{c_i}$, while being unmodified by the first collision step. Therefore,

$$n_0^*(\mathbf{r}_j,0)=16, \quad n_{1,\ldots,4}^*(\mathbf{r}_j,0)=4, \quad n_{5,\ldots,8}^*(\mathbf{r}_j,0)=1, \tag{26}$$

for $j=1,\ldots,8$.

The propagation step for the inner fluid nodes $(\mathbf{r}_2,\ldots,\mathbf{r}_7)$ does not involve the boundary rules and follows straightforwardly from Eq. (2):

$$n_{0,1,2}(\mathbf{r}_j,t+1)=n_{0,1,2}^*(\mathbf{r}_j,t),$$

$$n_{3,5,6}(\mathbf{r}_j,t+1)=n_{3,5,6}^*(\mathbf{r}_{j-1},t),$$

$$n_{4,7,8}(\mathbf{r}_j,t+1)=n_{4,7,8}^*(\mathbf{r}_{j+1},t), \tag{27}$$

for $j=2,\ldots,7$.

The nodes $\mathbf{r}_1$ and $\mathbf{r}_8$ need special treatment. The populations at $\mathbf{r}_8$ with velocities $\mathbf{c}_4$, $\mathbf{c}_7$, and $\mathbf{c}_8$ are determined by the link-bounce-back rule for a solid interface as given by Eq. (10): i.e.,

$$n_4(\mathbf{r}_8,t+1)=n_3^*(\mathbf{r}_8,t),$$

$$n_7(\mathbf{r}_8,t+1)=n_6^*(\mathbf{r}_8,t)+6U,$$

$$n_8(\mathbf{r}_8,t+1)=n_5^*(\mathbf{r}_8,t)-6U. \tag{28}$$

Similarly, the populations at $\mathbf{r}_1$ with velocities $\mathbf{c}_3$, $\mathbf{c}_5$, and $\mathbf{c}_6$ are determined by the new free-slip boundary condition for a fluid-gas interface as given by Eq. (11): i.e.,

$$n_3(\mathbf{r}_1,t+1)=n_4^*(\mathbf{r}_1,t),$$

$$n_5(\mathbf{r}_1,t+1)=n_8^*+\frac{1}{6}(n_1^*-n_2^*+n_5^*-n_6^*+n_7^*-n_8^*) - \frac{\lambda}{8}(n_1^{neq}+n_2^{neq}+n_5^{neq}+n_6^{neq}+n_7^{neq}+n_8^{neq}),$$

$$n_6(\mathbf{r}_1,t+1)=n_7^*-\frac{1}{6}(n_1^*-n_2^*+n_5^*-n_6^*+n_7^*-n_8^*) - \frac{\lambda}{8}(n_1^{neq}+n_2^{neq}+n_5^{neq}+n_6^{neq}+n_7^{neq}+n_8^{neq}). \tag{29}$$

For clarity, we omitted the arguments on the right-hand side of the last two equation which are all $(\mathbf{r}_1,t)$. Note that because of the particularly simple geometry, the update rule for n_3 is identical to that which would have been obtained by using the regular link-bounce-back rule.

TABLE I. The nine-velocity lattice-Boltzmann model.

i	a^{c_i}	$\mathbf{c}_i$
0	4/9	(0,0)
1,2	1/9	(±1,0)
3,4	1/9	(0,±1)
5,6	1/36	(±1,1)
7,8	1/36	(±1,−1)

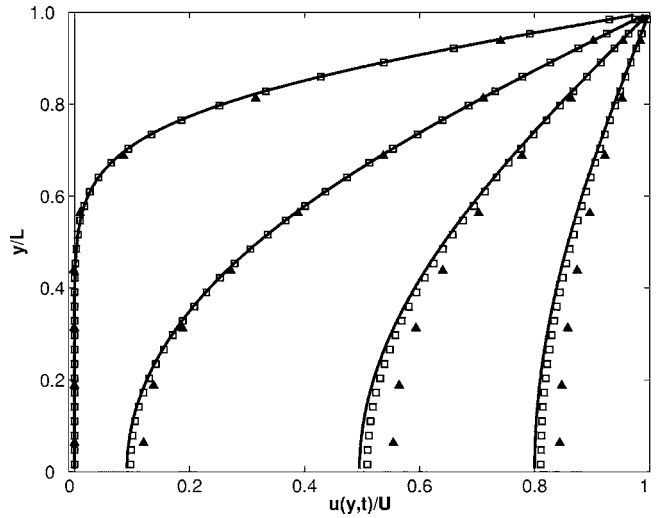

FIG. 2. Velocity profiles above an impulsively started plate at nondimensional times $\tau=\eta t/\rho L^2=1/64$, 1/8, 3/8, and 3/4 (from left to right). The fluid is bounded by a solid wall at $y/L=1$ and a free surface at $y=0$. The fluid density $\rho=36$, the wall velocity $U=10^{-3}$, and the viscosity $\eta=0.36$. The symbols are the lattice-Boltzmann results for $L=N=8$ (solid triangles) and $L=N=32$ (open squares). The solid lines are obtained from the Fourier-series solution [Eq. (25)] by truncating the series at $k=10\,000$.

Compare Eqs. (28) and (29) and one can see the difference between the bounce-back rule for a solid interface and the rule for a fluid-gas interface. There are three terms on the right-hand side of Eq. (29) (for n_5 and n_6). The first term originates from the regular bounce-back which is identical in both rules. The second term is proportional to the local fluid velocity parallel to the surface and is related to the second term in Eq. (23). The third term is proportional to the local fluid stress projected on the interface and is related to the third term in Eq. (23).

The remaining populations at node $\mathbf{r}_1$ and $\mathbf{r}_8$ follow the standard lattice-Boltzmann propagation rule, as in Eq. (27):

$$n_{0,1,2}(\mathbf{r}_1,t+1)=n^*_{0,1,2}(\mathbf{r}_1,t),$$

$$n_{4,7,8}(\mathbf{r}_1,t+1)=n^*_{3,6,5}(\mathbf{r}_2,t),$$

$$n_{0,1,2}(\mathbf{r}_8,t+1)=n^*_{0,1,2}(\mathbf{r}_8,t),$$

$$n_{3,5,6}(\mathbf{r}_8,t+1)=n^*_{3,5,6}(\mathbf{r}_7,t). \tag{30}$$

After resolving the propagation step and the boundary conditions, the populations at each node undergo collisions as determined by Eqs. (2), (8), and (9). The new populations are then ready for the next time step.

Figure 2 shows the development of the velocity profile in the gap. The velocities are obtained from the first moments of the n_i's [Eq. (1)]. Comparing the simulation with the Fourier series solution of Eq. (25), we see that using only eight fluid nodes already captures successfully the full transient behavior of flow field. Increasing the resolution to $L=N=32$ makes the numerical solution even more accurate. For $\eta t/\rho L^2\to\infty$, the numerical solution approaches the plug flow solution $u_x(y)/U=1$ (not shown in Fig. 2).

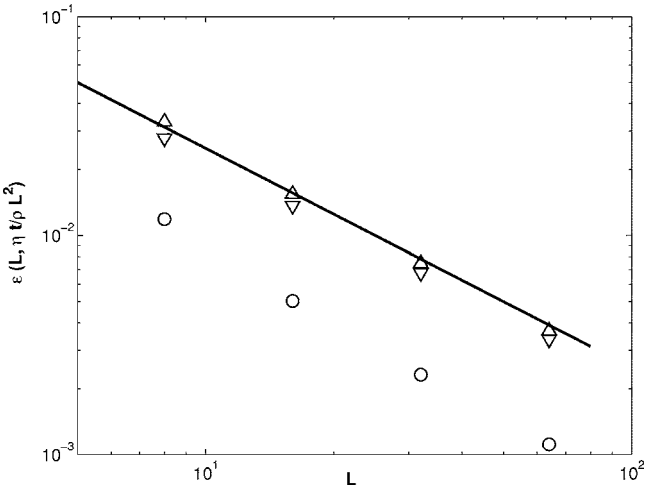

FIG. 3. Root-mean-square error $\epsilon(L,\tau)$ at nondimensional times $\tau=1/8(\bigcirc)$, $3/8(\triangle)$, and $3/4(\triangledown)$. The solid line represents the scale of L^{-1}. $L=8$, 16, 32, and 64.

The rate at which the errors decrease with increasing resolution can be observed from Fig. 3. The error is defined as

$$\epsilon(L,\tau)=\frac{1}{U}\left(\frac{1}{L}\sum_{\mathbf{r}\in L}[u_s(\mathbf{r},\tau)-u_x(\mathbf{r},\tau)]^2\right)^{1/2}, \tag{31}$$

where $\tau=\eta t/\rho L^2$ is the nondimensional time, $u_s(\mathbf{r},\tau)$ is the simulated velocity profile, and $u_x(y,t)$ is the velocity profile according to Eq. (25). The results shown in Fig. 3 are obtained using four different resolutions $L=N=8$, 16, 32, and 64. They indicate that $\epsilon(L,\tau)$ scales roughly as L^{-1}, which means our method is first-order accurate in lattice resolution.

B. Creeping flow past a cubic array of spherical bubbles

One of the great advantages of the link-bounce-back rule for the lattice-Boltzmann method is its ability to accurately handle curved interfaces and complex geometries with relative ease. By simulating the Stokes drag force on a cubic array of bubbles, we demonstrate here that this advantage also holds for our boundary conditions. In these simulations, a cubic array of bubbles is constructed by placing a single spherical bubble in a cubic computational domain and applying periodic boundary conditions in each direction. The bubble is then given a constant velocity U but its position is not advanced across the lattice. This artifice yields the correct fluid velocity and drag on the bubble owing to the quasisteady nature of Stokes flows. A pressure gradient is applied to the fluid with a value that is adjusted to ensure that the volume average velocity in the cubic cell (including the fluid and the bubble) is zero. We then calculated the total drag force F_D on the bubble from the exchange in momentum during the boundary node update [32]. The velocity U was chosen to be low enough to neglect any inertial effects, allowing us to compare our results with the theoretical prediction obtained by Sangani and Acrivos [45],

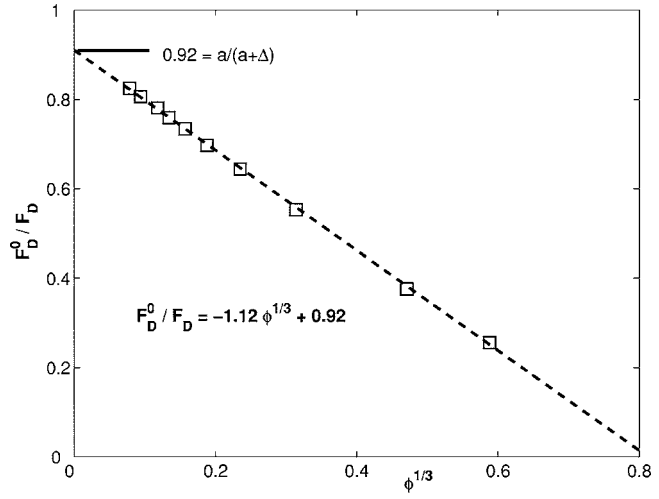

FIG. 4. Stokes drag force on a spherical bubble in a cubic array versus volume fraction for a bubble radius $a=2.92$, and velocity $U=10^{-4}$. F_D^0 is the Stokes drag force on an isolated bubble. The dashed line is a linear fit to the simulation data.

$$\frac{F_D(\phi)}{F_D^0} = \frac{1}{1 - 1.1734\phi^{1/3} - 0.1178\phi^2 + o(\phi^2)}, \quad (32)$$

where ϕ is the volume fraction and $F_D^0 = F_D(\phi=0)$ is the Stokes drag force on an isolated bubble,

$$F_D^0 = 4\pi\eta a U, \quad (33)$$

with a being the bubble radius. The fact that the drag force on a bubble in a cubic array is larger than that on an isolated bubble is due to the hydrodynamic interactions between the bubble and its periodic images. Note that the same procedure was used by Ladd [32] to simulate the Stokes drag force on a cubic array of spherical solid particles.

In Fig. 4, we summarize the results for a bubble radius $a=2.92$ and velocity $U=10^{-4}$. The fluid density and viscosity are $\rho=36$ and $\eta=6.0$, respectively. These parameters give $\mathrm{Re}=3.5\times10^{-3}$. Due to the discrete lattice, the drag force on a bubble varies slightly as the bubble's position changes relative to the underlying lattice. To minimize this discretization error, every data point is the average of four or five runs with each run using a randomly chosen position. The standard deviation in these runs relative to the mean value was 1% for the smallest bubble size and decreased with increasing resolution. Figure 4 shows that the simulations produce the correct $\phi^{1/3}$ scaling, with only a small deviation at the highest simulated volume fraction, due to the higher order terms in Eq. (32).

Figure 4 indicates that for a radius of 2.92, the respective relative error in the values of the slope and the intercept with the y axis is 5% and 8%. However, the accuracy can be improved considerably by a calibration process similar to that used in Ladd's solid-particle simulations [32]. This calibration process compensates for the fact that the link-bounce-back rule in Eq. (10) is only first-order accurate if the interface is not aligned with a lattice symmetry direction, resulting in a hydrodynamic boundary that is displaced from the physical boundary by an amount that depends on the orientation angle of the interface [41,46]. For an object with a curved interface such as a sphere, it is not possible to derive an analytical expression for the position of the hydrodynamic boundary. However, one can interpret the results in terms of the "effective" or "hydrodynamic" radius $a_H = a + \Delta$ rather than the input radius a (see Fig. 5), such that the drag coefficient on an isolated particle is identical to its theoretical value [47]. Ladd and Verberg [30] showed that this leads to approximate second-order accuracy in the lattice resolution and a reduction of the error in the drag force of approximately an order of magnitude. Furthermore, they found that Δ depends only on the particle radius and the fluid viscosity and not on the particle volume fraction, flow conditions, or Reynolds number, making it a well-defined physical parameter that can be obtained in a single calibration simulation.

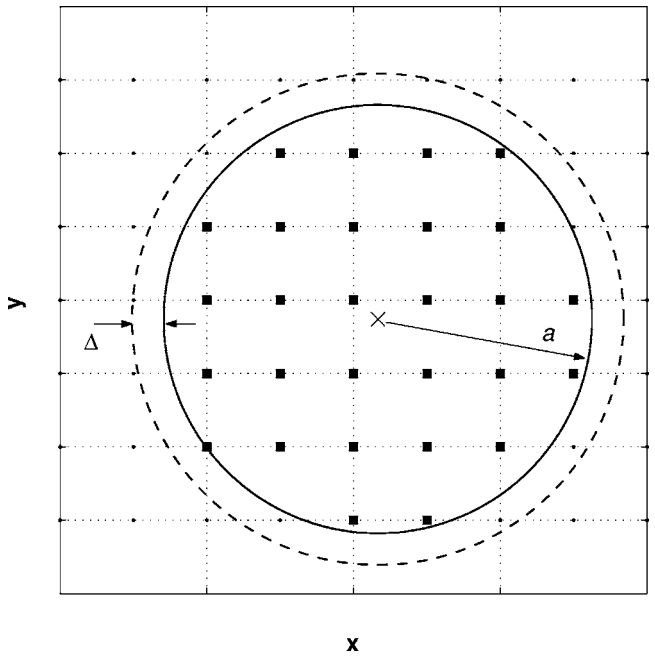

FIG. 5. A cross-sectional view of a spherical particle or bubble on the lattice-Boltzmann grid. The dots indicate the fluid nodes; the nodes inside the particle or bubble are marked by squares. The solid line is the interface for the input radius a and the dashed line that for the hydrodynamic radius $a_H = a + \Delta$.

The similarity between the link-bounce-back rule and our boundary rule for a fluid-gas interface suggests that calibrations for spherical bubbles can be carried out in a similar way. Hence, we determined a_H such that the Stokes drag force on a bubble in a cubic array of bubbles reduces in the dilute limit to its value for an isolated bubble—i.e., $F_D(\phi \to 0) = 4\pi\eta a_H U$. This implies that a/a_H can be identified from the intercept of $4\pi\eta a U / F_D(\phi)$ with the y axis (see Fig. 4). In Table II, we summarize the values that were obtained for a range of bubble radii and two viscosities, $\eta=6.0$ and $\eta=0.36$.

In Fig. 6, we plot the inverse of the ratio between the Stokes drag force on a bubble in a periodic array and that of an isolated bubble versus the bubble volume fraction, both rescaled in terms of the hydrodynamic radius—i.e., $F_{D,H}^0$

TABLE II. The hydrodynamic radii $a_H=a+\Delta$ for spherical bubbles for varying input radii a and viscosities η.

	$\eta=0.36$			$\eta=6.0$			
a	2.92	5.63	9.85	1.57	2.92	5.63	9.85
a_H	3.35	6.07	10.31	1.73	3.17	5.93	10.17
Δ	0.43	0.44	0.46	0.16	0.25	0.30	0.32

$=4\pi\eta a_H U$ and $\phi_H=4\pi a_H^3/3L^3$, with L being the size of the computational domain. The simulation results are now in excellent agreement with Eq. (32).

C. Intermediate-Reynolds-number flow around an isolated spherical bubble

The acceleration and steady rise of an isolated spherical bubble outside the creeping flow region have been studied extensively in the literature [1,25–29]. They provide therefore excellent opportunities to determine the accuracy of the method in the intermediate-Reynolds-number regime.

First, we briefly review the relevant results from previous work. We start with the drag force on a steadily rising bubble since it is easily measured and thus much better known than the forces on accelerating bubbles. When documenting the steady-state drag force on a spherical bubble, one usually expresses the results in terms of the dimensionless drag coefficient C_D,

$$C_D=\frac{F_D}{\frac{1}{2}\rho U_T^2\pi a_H^2}, \tag{34}$$

and the Reynolds number $\mathrm{Re}=(2\rho U_T a_H)/\eta$ based on the terminal velocity U_T. As the hydrodynamic correction improves

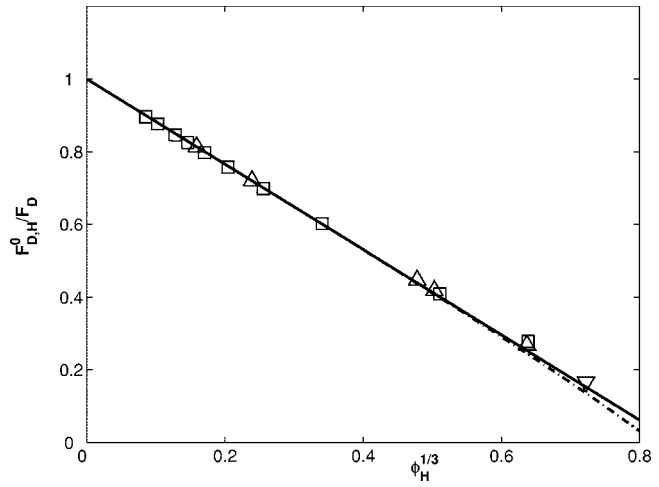

FIG. 6. Stokes drag force on a spherical bubble in a cubic array versus volume fraction ϕ_H rescaled in terms of the hydrodynamic radius. $F^0_{D,H}$ is the rescaled Stokes drag force on an isolated bubble. The lines are Sangani and Acrivos' theoretical prediction [45] [see Eq. (33)]. The solid line is their result up to order $\phi_H^{1/3}$; the dash-dotted line includes the ϕ_H^2 term. The symbols are the simulation results for $a_H=3.17(\square)$, $a_H=5.93(\triangle)$, and $a_H=10.31(\triangledown)$. The viscosity and bubble velocity are $\eta=6.0$ and $U=10^{-4}$.

the accuracy of the lattice-Boltzmann method, the hydrodynamic radius a_H, rather than the input radius a, is used consistently in this section. In the Stokes flow region, C_D and Re are related by

$$C_D=\frac{16}{\mathrm{Re}},\quad \mathrm{Re}\ll 1. \tag{35}$$

For small but finite Re, Kumagai [25] derived the Oseen correction to the Stokes flow result:

$$C_D=\frac{16}{\mathrm{Re}}\left(1+\frac{\mathrm{Re}}{8}\right), \tag{36}$$

which is found to agree reasonably well with the experimental results up to $\mathrm{Re}\approx 1$ [25]. For higher Reynolds numbers, Clift, Grace, and Weber [1] suggested the following correlation:

$$C_D=13.725\,\mathrm{Re}^{-0.74},\quad 4<\mathrm{Re}<100. \tag{37}$$

Finally, when Re is very large while the bubble remains spherical with the wake confined to a small region, we can assume potential flow in the entire fluid except for a thin boundary layer surrounding the bubble. The drag can then be determined analytically [5]:

$$C_D=\frac{48}{\mathrm{Re}}\left[1-\frac{2.21}{\mathrm{Re}^{1/2}}+O(\mathrm{Re}^{-5/6})\right],\quad \mathrm{Re}\gg 1. \tag{38}$$

The determination of the force on an accelerating spherical bubble is a much more difficult problem. To evaluate this force one must consider, in addition to the current acceleration, which gives rise to an added mass force, the forces due to the previous motion of the bubble. The latter contribution, known as the history integral, captures the effects of the transport and decay of the vorticity produced at the gas-liquid interface. Yang and Leal [26] first evaluated the history integral and derived the unsteady force on an accelerating spherical bubble in the creeping flow limit. Lovalenti and Brady [27] later used an Oseen point force and the reciprocal theorem to derive the unsteady force for small but finite Reynolds numbers. Based on numerical simulations and asymptotic analysis [48,49], Mei *et al.* [28] proposed a semi-analytical expression for the kernel of the history integral for a spherical bubble for $\mathrm{Re}>1$. The history integral was later used in a set of equations (Park *et al.* [29]) which predicts both the unsteady acceleration and the steady-state velocity of spherical bubbles for $0<\mathrm{Re}<300$. We compare our simulation results with the prediction of this set of equations. Since these equations are in rather lengthy forms, they are not included here. One can refer to Park *et al.* [29] for more details.

The lattice-Boltzmann simulations of rising bubbles in a fluid with inertia are set up differently from the creeping flow simulations in the previous section because we want to study the transient acceleration of the bubble as well as the final steady-state drag force. Moreover, at finite Reynolds numbers we can no longer assume the flow to be quasisteady, so it would be erroneous to give the bubble a constant velocity without accounting for the change in the bubble position. Thus, we took a more physical approach of releasing the

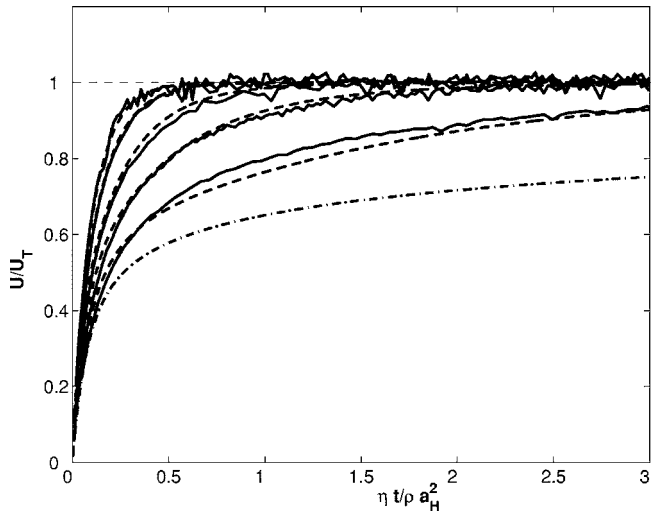

FIG. 7. The transient motion of spherical bubbles rising due to buoyancy for $L/a_H=23.88$. The solid lines are obtained from simulations, and the dashed lines are calculated using the equations given by Park *et al.* [29]. From upper left to lower right, the Archimedes numbers are 748.9, 451.1, 197.9, 87.8, and 27.0, corresponding to Reynolds numbers in the range $2<\mathrm{Re}<28$. The dash-dotted line represents the creeping flow limit [26].

bubble from a stationary position and letting it rise as a result of its buoyancy force. As in the previous simulations, a pressure gradient is applied to the fluid to assure that the mean velocity of the simulation cell is zero. Due to the initial imbalance of forces exerted on the bubble, it accelerates until the drag force, which increases with increasing velocity, equals the buoyancy force. Thereafter the bubble rises steadily, with only small fluctuations due to the discreteness of the underlying lattice. Since we cannot use the terminal velocity as an input parameter in these simulations, we use the Archimedes number to characterize our simulations. The Archimedes number, defined as

$$\mathrm{Ar}=\frac{8\rho^2 g a_H^3}{\eta^2}, \tag{39}$$

is independent of the bubble's velocity and characterizes the relative importance of gravitational (or buoyancy) forces and viscous forces.

The simulations were carried out in a cubic domain of dimension L with periodic boundary conditions. We used six Archimedes numbers, chosen such that they give Reynolds numbers of approximately 1, 2, 5, 10, 20, and 30. To determine whether the finite cell influenced the results, we used three values of L for each Archimedes number. To allow the bubble to sample all points relative to the lattice, the simulations were repeated 5–7 times with different orientations of the buoyancy force relative to the axes of the lattice. We avoided directions that were close to one of the primary lattice directions, since the drag force on a periodic array of bubbles is very different when the bubble is in the wake of its periodic images [50–52].

The acceleration of the bubble is shown in Fig. 7, where the bubble velocities are plotted as functions of time for a range of Archimedes numbers and the system size $L/a_H=23.88$. The velocities are normalized by the terminal velocity for each run, so that they all approach unity for $t\to\infty$. The time is nondimensionalized with $\rho a_H^2/\eta$. The simulation results are in good agreement with the predictions computed from the equations in Park *et al.* [29] for the four highest Archimedes numbers and the agreement is still reasonably good for $\mathrm{Ar}=27.0$ ($\mathrm{Re}\approx 2$). At this lower Reynolds number, the velocity disturbance produced by the periodic images of the bubble propagates over a large enough distance so that the hydrodynamic interactions between a bubble and its periodic images cannot be ignored. This leads to a relatively faster convergence to U_T than predicted by Park *et al.* [29]. This effect becomes less important as either the system size or the Reynolds number is increased. Indeed, there is no significant difference between the acceleration of bubbles with higher Archimedes numbers observed in cells of size $L/a_H=18.93$ and $L/a_H=23.88$. As the Archimedes number decreases, the time required for the bubble to reach its terminal velocity increases and the acceleration gradually approaches the creeping flow limit of $\mathrm{Re}\ll 1$. However, to accurately resolve the creeping flow behavior in a simulation of this kind would require a very large computational domain, because the final approach of the bubble velocity toward its terminal velocity is governed by momentum diffusion over very large distances.

We calculate Re and C_D from U_T and F_D, after the bubbles reach their terminal velocities. The results are summarized in Table III. For the two lowest Archimedes numbers ($\mathrm{Ar}=13.7$ and 27.0), the system size still has a noticeable effect on the results. For the higher Archimedes numbers, however, the results are virtually independent of system size for the range of L/a_H studied. For $\mathrm{Re}<10$, a bubble radius as small as $a_H=3.35$ is sufficient to keep the accuracy within ±3%. As Re is increased beyond 10, however, a larger lattice resolution is necessary to maintain the accuracy. In Fig. 8, one can see that the simulation results, plotted as C_D versus Re, agree well with Eqs. (35)–(37). The highest Reynolds number that we studied is still well below the lowest Reynolds number for which Eq. (38) applies; however, the simulations show a correct trend toward Eq. (38) with increasing Re.

V. CONCLUSION AND DISCUSSION

In this paper we presented a lattice-Boltzmann boundary rule for a fluid-gas interface. The rule recovers the free-slip boundary condition by modeling a bounce-back process for populations that cross the interface, which enforces a zero normal relative velocity and zero tangential stress condition at the fluid-gas interface. A two-dimensional test for flow driven by an impulsively started plate with a free surface above showed that the rule accurately accounts for both steady and unsteady flows near a flat interface.

This lattice-Boltzmann model is an ideal tool to simulate a special class of multiphase flows involving nearly spherical, noncoalescing bubbles. By treating the bubbles as spheres with a free-slip boundary condition imposed on the

TABLE III. The drag coefficients and terminal Reynolds numbers of bubbles for a range of Archimedes numbers. The two columns in the center are the simulation results with the numbers in the brackets representing the standard deviations of successive runs with different orientations. The last two columns are the steady-state values calculated from the equations given in [29]. All simulations were carried out with a bubble radius a_H=3.35 and a fluid viscosity η=0.36 except for (i) a_H=3.17 and η=6.0 (result is viscosity independent) and (ii) a_H=6.07 and η=0.36 (for Re$>$10 a larger radius gives more accurate results).

Ar	L/a_H	Re	C_D	Re	C_D
	11.94	0.943 (0.005)	20.6 (0.2)		
13.7	17.92	0.992 (0.004)	18.6 (0.2)	1.037	17.0
	23.88	1.010 (0.005)	17.9 (0.2)		
13.8[i]	18.93	0.996 (0.003)	18.5 (0.1)	1.040	17.0
	11.94	1.81 (0.02)	11.0 (0.2)		
27.0	17.92	1.852 (0.004)	10.52 (0.04)	1.92	9.76
	23.88	1.89 (0.02)	10.1 (0.2)		
	11.94	5.09 (0.09)	4.52 (0.16)		
87.8	17.92	5.23 (0.05)	4.28 (0.08)	5.35	4.10
	23.88	5.26 (0.03)	4.23 (0.05)		
	11.94	10.0 (0.1)	2.64 (0.07)		
197.9	17.92	10.22 (0.06)	2.53 (0.02)	10.54	2.38
	23.88	10.22 (0.08)	2.53 (0.01)		
198.6[ii]	13.18	10.3 (0.1)	2.51 (0.06)	10.57	2.37
	19.77	10.46 (0.04)	2.42 (0.02)		
	11.94	18.8 (0.1)	1.69 (0.02)		
451.1	17.92	19.1 (0.1)	1.65 (0.02)	20.9	1.38
	23.88	19.4 (0.1)	1.60 (0.02)		
	11.94	27.6 (0.4)	1.31 (0.04)		
748.9	17.92	27.9 (0.5)	1.28 (0.05)	31.9	0.98
	23.88	28.1 (0.5)	1.26 (0.05)		
747.9[ii]	13.18	29.4 (0.2)	1.16 (0.02)	31.8	0.98
	19.77	29.81 (0.05)	1.122 (0.004)		

surface, we only need to simulate the flow in the continuous phase. Numerical tests of flows around three-dimensional bubbles showed that our model can accurately solve transient and steady flows around spherical bubbles for Reynolds numbers in the range $0<\mathrm{Re}<30$. Hence, our model allows for efficient simulation of bubbly suspensions in the intermediate-Reynolds-number regime, making it possible to bridge the gap in between previous studies of purely viscous and purely inertia-dominated flows [3,4,8–14].

Compared with bubble simulations that use two immiscible fluids, the direct simulation of the free-slip boundary condition offers several advantages. First, neglecting the gas component reduces the computational cost. Second, the numerical difficulty of employing two fluids with vastly different densities and viscosities can be avoided. Third, the complex geometry associated with moving interfaces can be treated with relative ease due to the simple nature of the single-component lattice-Boltzmann bounce-back rule. Although we limited ourselves in this work to spherical bubbles, our boundary rule applies equally well, and without modifications, to other shapes. Furthermore, after coupling our method to a correct surface tension model, our boundary rule may be used to simulate deformable bubbles in the future.

While we did not carry out systematic studies on the stability of the algorithm, we found that the planar flow example is remarkably stable. A stable solution was obtained even at η=0.012, which was the lowest viscosity tested. There were no signs of numerical instability for the three-dimensional bubble simulations at the dynamic viscosity 0.36 used for those studies.

Because a molecule undergoing a specular reflection from a surface experiences no change in its tangential momentum, it would be natural to consider developing a no-tangential-stress boundary condition based on specular reflection. Indeed, there are several papers on rarefied gas flows in microchannels, where a hybrid scheme of specular reflection and regular bounce-back was applied on stationary, planar interfaces to simulate the partial velocity slip due to the finite-Knudsen-number effect [53–56]. We also tested such an approach during the early stages of our study. However, in practice we found that specular reflection only works when the interface is aligned with the lattice directions, such as the planar flow example discussed in Sec. IV A, and does not maintain a stationary solution near an oblique interface.

Consider a special example where there is a slip interface that is aligned with the lattice direction, as illustrated in Fig. 9(a). Both the interface and fluid above the interface are at

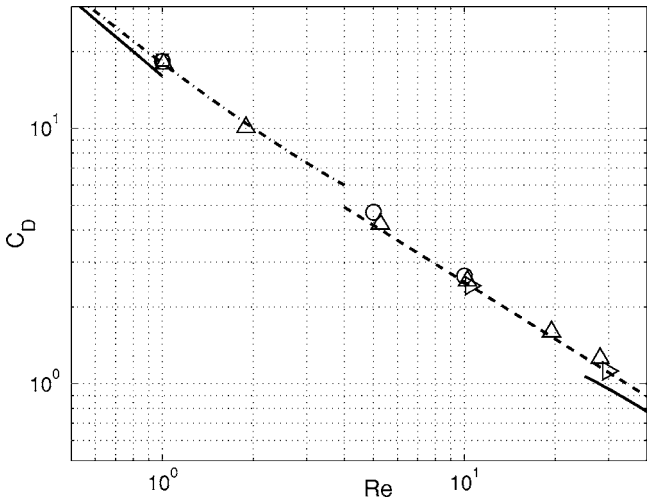

FIG. 8. Drag coefficient C_D as a function of the Reynolds number. The symbols represent the simulation data. For clarity, for a given Ar only the largest L/a_H data are shown. The viscosity is $\eta=0.36$ unless otherwise mentioned. (△) $L/a_H=23.88$; $a_H=3.35$; (▷) $L/a_H=19.77$; $a_H=6.07$; (□) $L/a_H=18.93$; $a_H=3.17$; $\eta=6.0$; (○) experimental measurements of deformable bubbles, cited in [1]. The solid line in the upper left corner represents the Stokes drag, Eq. (35); the dash-dotted line is the Oseen solution, Eq. (36); the dashed line the correlation, Eq. (37); and the solid line on the lower right corresponds to Moore's solution for high Re Eq. (38).

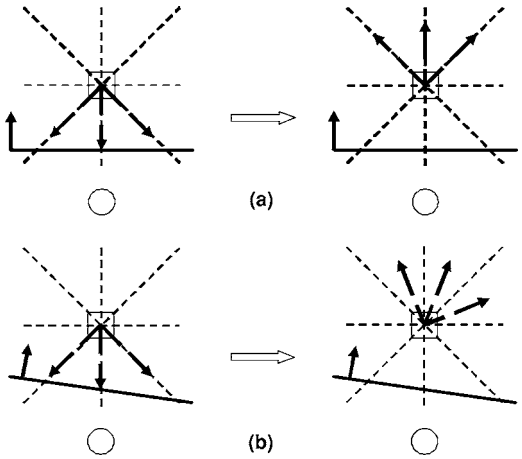

FIG. 9. Specular reflection of populations near (a) an interface aligned with a lattice direction and (b) an oblique interface not aligned with any lattice direction. (□) represents a fluid node and (○) represents a node outside the fluid. The thick solid line between the two nodes is the interface with an arrow representing the surface normal. The populations that collide with the interface are represented by the dashed arrows. They follow Table I and satisfy $n_i=\rho a^{c_i}$. The short-dashed lines represent the lattice directions. In (b), the reflected populations are skewed. The zeroth, first, and second moments of the reflected populations do not preserve the stationary solution $n_i=\rho a^{c_i}$ near an oblique interface.

rest; thus, everywhere in the fluid the distribution is stationary: $n_i=\rho a^{c_i}$. In the propagation and boundary collision step, the populations that collide with the interface, n_4, n_7, and n_8, are specularly reflected to 3, 5, and 6 directions. The populations propagated from neighbor fluid nodes now occupy 1, 2, 4, 7, and 8 directions. Since $n_i=\rho a^{c_i}$ is still satisfied, the post-collision distribution n_i^* remains stationary.

When the interface is not aligned with the lattice directions, as shown in Fig. 9(b), the specularly reflected populations from n_4, n_7, and n_8 are skewed and are no longer in the 3, 5, and 6 directions. Since the velocities of the reflected molecules are not in lattice directions, some scheme is required so that the reflected molecules propagate on the lattice. We required that the molecules return to the same fluid node after the reflection. One can then use the zeroth, first, and second moments of the velocity of molecules arriving at the node from the interface and from other fluid nodes in a collision operator for this fluid node. However, such a scheme does not preserve the equilibrium velocity distribution in a fluid at rest in the presence of a stationary interface. In contrast, the bounce-back boundary condition [Eq. (24)] developed here is designed specifically to preserve any velocity distribution function that is consistent with the no tangential stress and no normal velocity boundary conditions, irrespective of the angle between the surface normal and the underlying lattice directions.

Similar to the link-bounce-back rules for solid-liquid interfaces, our boundary rule always assumes that the gas-liquid interface is represented by boundary nodes that are halfway between gas and fluid nodes. More accurate representations of the boundary can be obtained either via volumetric approaches [40,57–59] or interpolations [42,60,61]. Among others, Bouzidi *et al.* [60] have proposed an improved bounce-back method based on interpolation to impose the slip boundary condition at an arbitrary distance from a fluid node instead of 1/2. In general, when the interface is not located at 1/2 positions, the populations that start at fluid nodes and collide with the interface will not be bounced back to the original nodes. Thus, to prepare for the collision step, it is necessary to calculate the populations at the original nodes via linear or quadratic interpolations. Since our method for the slip boundary condition is a special type of bounce-back rule, it is possible to use ideas similar to those developed in [60] to derive rules to improve the spatial accuracy. However, such an interpolation would always require additional information, such as the surface normals and the positions where the interface cuts the lattice links, making the method substantially more complicated. The determination of these structural parameters in an evolving geometry such a bubble suspension would incur substantial computational costs.

ACKNOWLEDGMENTS

This work was supported by NASA under Grant No. NAG3-1853. The computational resources were provided by the Cornell Theory Center.

[1] R. Clift, J. R. Grace, and M. E. Weber, *Bubbles Drops and Particles* (Academic Press, New York, 1978).
[2] R. R. Lessard and S. A. Zieminski, Ind. Eng. Chem. Fundam. **10**, 260 (1971).
[3] R. Zenit, D. L. Koch, and A. S. Sangani, J. Fluid Mech. **429**, 307 (2001).
[4] G. Mo and A. S. Sangani, Phys. Fluids A **6**, 1637 (1993).
[5] D. W. Moore, J. Fluid Mech. **16**, 161 (1963).
[6] D. W. Moore, J. Fluid Mech. **23**, 749 (1965).
[7] P. C. Duineveld, J. Fluid Mech. **292**, 325 (1995).
[8] A. Biesheuvel and L. Van Wijngaarden, J. Eng. Math. **16**, 349 (1982).
[9] A. S. Sangani and A. K. Didwania, J. Fluid Mech. **250**, 307 (1993).
[10] D. Z. Zhang and A. Prosperetti, J. Fluid Mech. **267**, 185 (1994).
[11] H. F. Bulthuis, A. Prosperetti, and A. S. Sangani, J. Fluid Mech. **294**, 1 (1995).
[12] Y. Yurkovetsky and J. F. Brady, Phys. Fluids **8**, 881 (1995).
[13] S.-Y. Kang, A. S. Sangani, H.-K. Tsao, and D. L. Koch, Phys. Fluids **9**, 1540 (1997).
[14] P. D. M. Spelt and A. S. Sangani, Appl. Sci. Res. **58**, 337 (1998).
[15] A. Esmaeeli and G. Tryggvason, J. Fluid Mech. **377**, 313 (1998).
[16] A. Esmaeeli and G. Tryggvason, J. Fluid Mech. **385**, 325 (1999).
[17] B. Bunner and G. Tryggvason, J. Fluid Mech. **466**, 17 (2002).
[18] B. Bunner and G. Tryggvason, J. Fluid Mech. **466**, 53 (2002).
[19] K. Sankaranarayanan, X. Shan, I. G. Kevrekidis, and S. Sundaresan, Chem. Eng. Sci. **54**, 4817 (1999).
[20] K. Sankaranarayanan, X. Shan, I. G. Kevrekidis, and S. Sundaresan, J. Fluid Mech. **452**, 61 (2002).
[21] K. Sankaranarayanan and S. Sundaresan, Chem. Eng. Sci. **57**, 3521 (2002).
[22] J. Tölke, M. Krafczyk, M. Schulz, and E. Rank, Philos. Trans. R. Soc. London, Ser. A **360**, 535 (2002).
[23] T. Inamuro, T. Ogata, S. Tajima, and N. Konishi, J. Comput. Phys. **198**, 628 (2004).
[24] A. J. Wagner, Int. J. Mod. Phys. B **17**, 193 (2003).
[25] T. Kumagai, Bull. JSME **29**, 3367 (1986).
[26] S.-M. Yang and L. G. Leal, Phys. Fluids A **3**, 1822 (1991).
[27] P. M. Lovalenti and J. F. Brady, Phys. Fluids A **5**, 2104 (1993).
[28] R. Mei, J. F. Klausner, and C. J. Lawrence, Phys. Fluids **6**, 418 (1994).
[29] W. C. Park, J. F. Klausner, and R. Mei, Exp. Fluids **19**, 167 (1995).
[30] A. J. C. Ladd and R. Verberg, J. Stat. Phys. **104**, 1191 (2001).
[31] S. Chen and G. D. Doolen, Annu. Rev. Fluid Mech. **30**, 329 (1998).
[32] A. J. C. Ladd, J. Fluid Mech. **271**, 285 (1994).
[33] A. J. C. Ladd, J. Fluid Mech. **271**, 311 (1994).
[34] U. Frisch, D. d'Humières, B. Hasslacher, P. Lallemand, Y. Pomeau, and J.-P. Rivet, Complex Syst. **1**, 649 (1987).
[35] X. He and L.-S. Luo, J. Stat. Phys. **88**, 927 (1997).
[36] Y. H. Qian, D. d'Humières, and P. Lallemand, Europhys. Lett. **17**, 479 (1992).
[37] H. Chen, S. Chen, and W. H. Matthaeus, Phys. Rev. A **45**, R5339 (1992).
[38] S. Chen, Z. Wang, X. Shan, and G. D. Doolen, J. Stat. Phys. **68**, 379 (1992).
[39] D. d'Humières, I. Ginzburg, M. Krafczyk, P. Lallemand, and L.-S. Luo, Philos. Trans. R. Soc. London, Ser. A **360**, 437 (2002).
[40] R. Verberg and A. J. C. Ladd, Phys. Rev. Lett. **84**, 2148 (2000).
[41] I. Ginzbourg and D. d'Humières, J. Stat. Phys. **84**, 927 (1996).
[42] R. Mei, L.-S. Luo, and W. Shyy, J. Comput. Phys. **155**, 307 (1999).
[43] S. Chen, D. Martinez, and R. Mei, Phys. Fluids **8**, 2527 (1996).
[44] X. He, Q. Zou, L.-S. Luo, and M. Dembo, J. Stat. Phys. **87**, 115 (1997).
[45] A. S. Sangani and A. Acrivos, Int. J. Multiphase Flow **9**, 181 (1983).
[46] I. Ginzbourg and P. M. Adler, J. Phys. II **4**, 191 (1994).
[47] H. Hasimoto, J. Fluid Mech. **5**, 317 (1959).
[48] R. Mei and J. F. Klausner, Phys. Fluids A **4**, 63 (1992).
[49] R. Mei and R. J. Adrian, J. Fluid Mech. **237**, 323 (1992).
[50] D. L. Koch and A. J. C. Ladd, J. Fluid Mech. **349**, 31 (1997).
[51] R. J. Hill, D. L. Koch, and A. J. C. Ladd, J. Fluid Mech. **448**, 213 (2001).
[52] R. J. Hill, D. L. Koch, and A. J. C. Ladd, J. Fluid Mech. **448**, 243 (2001).
[53] C. Y. Lim, C. Shu, X. D. Niu, and Y. T. Chew, Phys. Fluids **14**, 2299 (2002).
[54] S. Succi, Phys. Rev. Lett. **89**, 064502 (2002).
[55] Y. Zhang, R. Qin, and D. R. Emerson, Phys. Rev. E **71**, 047702 (2005).
[56] L. Zhu, D. Tretheway, L. Petzold, and C. Meinhart, J. Comput. Phys. **202**, 181 (2005).
[57] H. Chen, Phys. Rev. E **58**, 3955 (1998).
[58] H. Chen, C. Teixeira, and K. Molvig, Int. J. Mod. Phys. C **8**, 1281 (1998).
[59] R. Verberg and A. J. C. Ladd, Phys. Rev. E **65**, 016701 (2001).
[60] M. Bouzidi, M. Firdaouss, and P. Lallemand, Phys. Fluids **13**, 3452 (2001).
[61] P. Lallemand and L.-S. Luo, J. Comput. Phys. **184**, 406 (2003).